nature communications

Article | Article in Press

https://doi.org/10.1038/s41467-026-78862-6

Thin-film lithium tantalate for ultraviolet integrated electro-optic modulator

Received: 28 May 2026

Accepted: 6 October 2026

Published online: 27 October 2026

Check for updates

Chupao Lin[1] ✉, Patrick Nenezic[1], Arno Moerman[2], Simone Cammarata[2], Simone Atzeni[1], Konstantinos Akritidis[1], Tom Vanackere[1], Margot Niels[1], He Li[1], Valeria Bonito Oliva[1], Xin Yin[2], Maximilien Billet[1] & Bart Kuyken[1]

The realization of integrated, high-speed ultraviolet modulation is pivotal for the advancement of quantum information processing, portable atomic clocks, and secure solar-blind communications. While mature photonic platforms have enabled sophisticated system-level integration across the visible and infrared spectral ranges, high-speed active modulation in the ultraviolet remains largely dependent on conventional bulk-crystal technologies. Consequently, a scalable integrated solution that simultaneously combines low insertion loss and extreme compactness with high modulation efficiency has remained challenging. Here, we report an integrated UV electro-optic modulator on a thin-film lithium tantalate platform. The device has a compact lumped-electrode of 200 μm, exhibiting a measured 3 dB electrical-to-optical-to-electrical bandwidth above 40 GHz, a high modulation efficiency $V_\pi L$ of 85 mV · cm, and a measured electrical-to-electrical bandwidth beyond 67 GHz. This work establishes thin-film lithium tantalate as a disruptive platform for wafer-scale compatible active UV photonics, enabling the next generation of scalable quantum and communication systems.

Precise manipulation of ultraviolet (UV) and visible light is fundamental to a diverse range of emerging technologies, as illustrated in Fig. 1. These include trapped-ion quantum computing and optical clocking[1–3], high-precision UV spectroscopy[4], high throughput microscopy[5,6], solar blind communications[7] and underwater optical communication[8]. To date, UV optical architectures have relied predominantly on discrete bulk components, such as mirrors, lenses, and macroscopic modulators. However, this bulk-optical approach is inherently limited by poor scalability and high sensitivity to mechanical vibrations. Shifting toward an integrated photonic platform not only enables high-fidelity control over the amplitude, frequency, and phase of light but also fundamentally suppresses ambient control noise through a more robust and compact footprint[9]. Driven by the need for telecommunications, platforms like silicon (Si) and silicon nitride (SiN_x) have facilitated complex system-level integration at infrared wavelengths. Yet, this success has not translated to the UV regime, as the limited bandgaps of these materials fundamentally lead to prohibitive absorption in UV. The emergence of the photonic platform based on thin-film alumina (AlO_x) provides a scalable architecture for large-scale passive photonic integration in UV[10,11]. However, this platform lacks intrinsic gain media and a second-order (χ^2) nonlinearity. Consequently, active functionality has been primarily restricted to thermo-optic (TO) phase shifters. While TO modulation is a well-established mechanism for tuning phase and intensity, its operation is fundamentally constrained by slow response times (on the order of 10 s of kHz[12]) and significant thermal crosstalk, both of which severely limit the attainable modulation bandwidth and circuit integration density. In the telecommunication bands, silicon photonics has demonstrated high-speed modulation up to the tens of GHz regime[13]. In contrast, UV photonic platforms have not yet reached such maturity. Establishing a robust, high-speed active component library is essential to bridge this gap and unlock the full potential of UV photonic platforms. Realizing high-speed UV modulation remains a challenge, primarily due to the lack of low-loss thin films with significant electro-

[1]Department of Information Technology (INTEC), Photonics Research Group, Ghent University - imec, Ghent, Belgium. [2]Department of Information Technology (INTEC), IDLab, Ghent University-imec, Ghent, Belgium. ✉e-mail: Chupao.Lin@UGent.be

https://doi.org/10.1038/s41467-026-78862-6

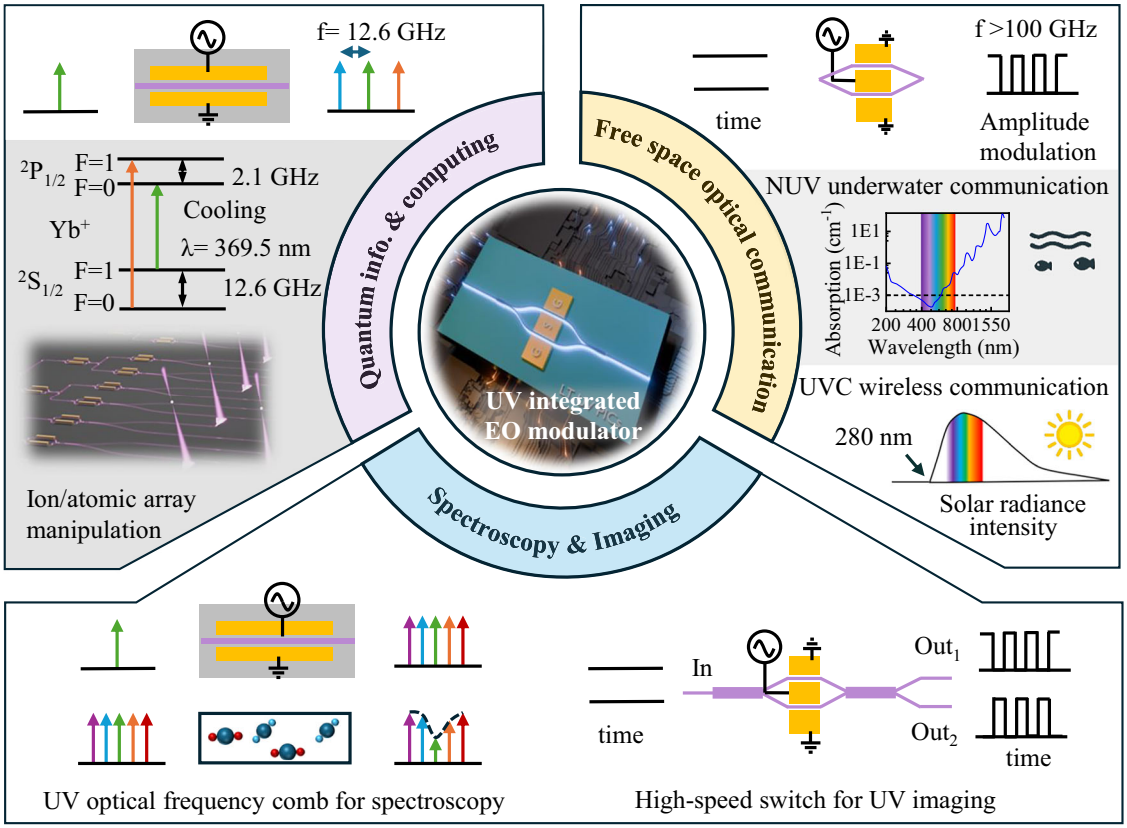


Fig. 1 | Potential applications of high-speed UV integrated electro-optic modulators.

optic (EO) coefficients. While the platform of aluminum nitride (AlN) on sapphire offers a wide bandgap and a modest EO coefficient (~1 pm/V), its potential for UV photonic integrated circuits (PICs) is severely hampered by the lattice mismatch at the AlN-sapphire interface. This structural disparity induces high material absorption and scattering losses[14], fundamentally obstructing its integration into high-performance UV circuits. Alternatively, by leveraging the strong piezoelectric coefficient of aluminum nitride, Castillo et al.[15] recently integrated AlN piezo-optomechanical actuators with AlO_x resonators. This architecture achieves intensity modulation of UV light at frequencies reaching the tens of MHz. However, the modulation bandwidth is inherently governed by the mechanical resonance frequencies of the actuator. Achieving gigahertz-rate integrated UV modulation is a critical milestone that will enable a suite of applications currently restricted to laboratory-scale, bulk-optical setups. For instance, a phase modulation frequency of 12.6 GHz is fundamental for addressing the hyperfine transitions of $^{171}Yb^+$ ions at 369.5 nm. Besides, high speed optical modulation enables large bandwidth data transmission (>100 GHz) for wireless UV communication. It also allows tuning the density of EO frequency comb lines, from tens of MHz to tens of GHz, for high-speed spectroscopy applications[16]. Currently, high-speed UV phase modulation relies on bulk electro-optic crystals such as β-barium borate (BBO) and deuterated potassium dihydrogen phosphate (DKDP)[17–19]. However, their macroscopic geometry and wide electrode gaps necessitate half-wave voltages (V_π) on the order of kilovolts. This requirement imposes a severe bottleneck: the high-power RF drive needed to reach GHz frequencies induces substantial resistive heating, effectively restricting the sustainable intensity modulation rate to the hundreds of MHz regime. Despite the maturity of high-speed modulation in the near-infrared, a high-speed UV counterpart has remained challenging due to a main conflict: the difficulty of realizing a thin-film platform that simultaneously provides a high electro-optic coefficient, low propagation loss, and a wafer-scale compatible fabrication process.

Thin film lithium niobate (TFLN) has emerged as a workhorse for integrated EO modulators in the telecommunication bands due to its high Pockels coefficient of $r_{33} \approx 30$ pm/V at 1550 nm. Recent advances have extended this performance into the visible spectrum. By optimizing traveling-wave electrode architectures, TFLN platforms have achieved a low half-wave voltage-length product ($V_\pi L$) of 0.17 V · cm at 450 nm with 3-dB bandwidths exceeding 20 GHz[20,21], as well as bandwidths surpassing 50 GHz at 493 nm[22]. This makes TFLN a potential material platform for achieving high-speed modulation in the near−UV range. For instance, it has recently demonstrated milliwatt-level power handling at a wavelength of 390 nm[23]. However, the fundamental bandgap of $LiNbO_3$ and the photorefractive effect, which causes optical damage and instability at high photon energies, severely hinder its application in the UV and deep-blue regimes[24–26]. In contrast, thin-film lithium tantalate (TFLT) presents a compelling alternative for UV applications. While maintaining a high electro-optic coefficient comparable to TFLN, TFLT extends optical transparency down to 275 nm[27,28]. Crucially, it exhibits a significantly suppressed photorefractive effect compared to its niobate counterpart, providing the requisite power stability and damage resistance for high-intensity UV photonic integration[24,25]. The photorefractive index change Δn of TFLT is below 10^{-6}, an order of magnitude lower than that of TFLN (1.4×10^{-5}) at a power intensity of 13 kW/cm^2 and a wavelength of 532 nm. Furthermore, TFLT features a low thermo-optic coefficient on the order of 10^{-6}/K [29], an order of magnitude smaller than that of TFLN [30]. While TFLT-based EO modulators have recently been demonstrated across the near-infrared and visible spectra[31,32], their extension into the UV remains an open challenge. This is primarily attributed to the dramatic increase in Rayleigh scattering, which scales as $1/\lambda^4$ and becomes the

https://doi.org/10.1038/s41467-026-78862-6

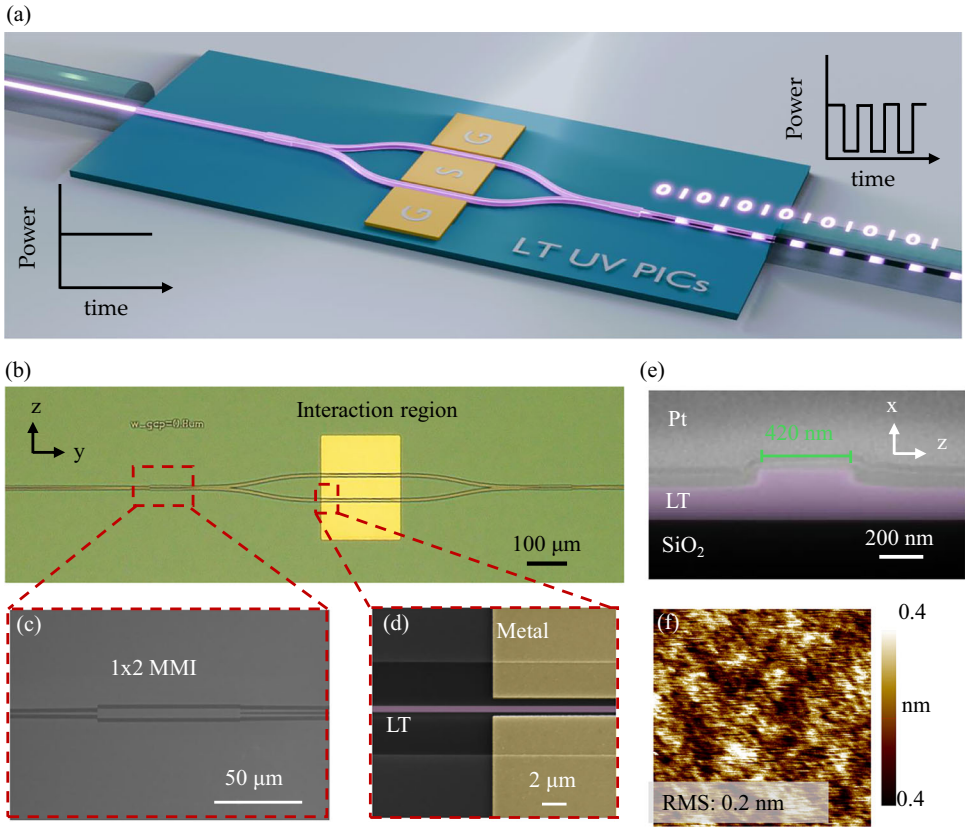


Fig. 2 | Concept of lithium tantalate (LT) UV modulator. a Schematic of integrated thin-film lithium tantalate UV modulator. **b** Optical image of the fabricated device. **c** Scanning electron microscopy image of a 1 × 2 multi-mode interferometer. The length of the interaction region is 200 μm. **d** Scanning electron microscopy image of the electrode and LT waveguide. The gap between signal and ground electrodes is 1.5 μm. **e** Cross-section image of the LT waveguide with a tilt angle of 52 degrees. The arrows indicate the crystal axis of lithium tantalate. **f** Atomic force microscopy image of the etched LT waveguide surface. The surface roughness root-mean-square (RMS) is measured to be 0.2 nm over the scanning area of 5 × 5 μm^2.

dominant loss mechanism at shorter wavelengths. Furthermore, while the sub-surface crystal defects induced by the hydrogen ion-slicing process are negligible in the visible/NIR regime, they likely act as absorption and scattering centers in the UV, where photon energies approach the electronic transitions of these defect states. Single mode LT waveguide shows propagation loss up to 4 dB/cm at a visible wavelength of 532 nm, which is much higher than that in NIR wavelength of 0.5 dB/cm waveguide[26]. This rapid increase in attenuation trend suggests that achieving a low propagation loss of several dB/cm remains challenging at UV wavelengths.

In this work, we demonstrate a high-performance integrated modulator based on a TFLT platform operating in the UV. We report the realization of a single-mode LT waveguide at $\lambda = 375$ nm with a propagation loss of 7.2 dB/cm. This modulator exhibits low insertion loss of 2.8 dB, ultra compact modulation length of 200 μm, low $V_\pi L$ of 85 mV · cm and beyond 40 GHz electrical-to-optical-to-electrical (EOE) modulation bandwidth. To the best of our knowledge, this represents the integrated UV electro-optic modulator that simultaneously achieves low insertion loss, compact device footprint, and tens of gigahertz modulation rates, which has not been demonstrated. This platform outperforms conventional bulk-crystal architectures, offering a two-order-of-magnitude reduction in $V_\pi L$ and a scalable path for complex UV photonic circuits. By providing a robust, high-speed solution for UV integrated photonics, this platform establishes a scalable architecture for the next generation of quantum information processors, ultra-precise atomic clocks, and high-bandwidth non-line-of-sight (NLOS) communication systems.

Results

Device design and implementation

The strong electro-optic response of lithium tantalate enables efficient, high-speed phase modulation of the guided optical modes. While both microring resonators and Mach-Zehnder interferometers (MZIs) are widely used for integrated modulation, we employ an MZI architecture to ensure operational robustness. Unlike resonator-based modulators, which are highly sensitive to thermal fluctuations and fabrication errors, the MZI offers broadband operation and eliminates the need for complex, active resonance stabilization—a critical advantage for stable UV photonics. The architecture of our integrated TFLT UV modulator is schematically illustrated in Fig. 2a. The MZI features a dual-arm phase modulator in a push-pull configuration driven by a ground-signal-ground (GSG) lumped electrode, where the applied electric field induces refractive index changes of opposite signs in each arm. This differential phase shift effectively doubles the total phase accumulation for a given bias, thereby halving the half-wave voltage (V_π) and enhancing the modulation efficiency. In this work, a 375 nm UV source (Bios375-20FC, Elite optoelectronics co. ltd) is coupled via a cleaved single-mode fiber (SM300, Thorlabs) into the polished LT chip. The LT waveguide facets are tapered to 2.7 μm to minimize modal mismatch and enhance coupling efficiency to a simulated fiber-to-waveguide loss of 7.5 dB per facet. The experimentally measured coupling loss is 9.7 ± 0.3 dB/facet. The coupling loss can be further minimized by implementing spot-size converters, a strategy previously demonstrated on TFLN at telecom wavelengths[33] and on AlO_x in the UV[34]. A 1 × 2 multi-mode interferometer (MMI) splits the light equally into two arms. Both beams are then modulated by the

phase shifter before interfering at a second, symmetric 1 × 2 MMI. The resulting signal is coupled back into a single-mode fiber. The combination of a high EO coefficient and a short working wavelength enables an exceptionally compact device footprint. A modulation length of only 200 µm is sufficient to reach a 2π phase shift at a CMOS-compatible driving voltage of 4.2V. This ultra-compact interaction length is two orders of magnitude smaller than those typically required at telecommunication wavelengths. This disparity highlights the inherent scaling advantage of the UV regime: because the induced phase shift ($\Delta\phi = 2\pi L\Delta n/\lambda$) is inversely proportional to wavelength, the modulation effect is naturally magnified as λ decreases. The length of the modulator is 1.16 mm (Fig. 2b), representing a highly footprint-efficient solution for UV integrated photonics compared to traditional bulk components. Scanning electron microscopy (SEM) images in Fig. 2c, d provide magnified views of the MMI and the phase modulator input, respectively. A narrow electrode gap of 1.5 µm was used to maximize the electric field strength and modulation efficiency, while minimizing metal-induced optical losses. The PICs were patterned on a commercial 300 nm-thick x-cut LT-on-insulator platform with a 100 nm etch depth. The TFLT platform provides high index contrast, which is essential for tight mode confinement and the realization of small-footprint UV circuits. To ensure single-mode operation, critical for maintaining high extinction ratios (ER) in the MZI, the waveguide width is tapered from 2.70 µm to 0.42 µm. Figure 2e shows a SEM cross-section of the waveguide. A platinum layer was deposited prior to imaging to mitigate charging effects caused by the insulating substrate. Vertical sidewalls were achieved via wet chemical etching using a mixture of H_2O_2/KOH/$C_6H_8O_7$[35]. Minimizing surface roughness is critical to reducing scattering and propagation losses, which scale as $1/\lambda^4$ and are therefore significantly more detrimental at 375 nm than at infrared wavelengths. Atomic force microscopy (AFM) measurements, reported in Fig. 2f, confirmed a smooth etched surface with a root-mean-square (RMS) roughness of 0.2 nm over a 5 × 5 µm^2 area, demonstrating the high precision of our fabrication process in achieving sub-nanometer surface quality.

Passive device characterization

The passive optical performance of the device was evaluated through a comprehensive loss characterization. The propagation loss was characterized using a set of spirals of different lengths. To mitigate the effects of anisotropic wet etching, where lateral etch rates depend on the crystal plane, pre-compensation is applied to the width of spiral characterization waveguides to reduce the bend loss due to the width variation. The device architecture is optimized for the TE mode, with propagation along the y-axis to leverage the crystal's r_{33} coefficient (aligned with the z-axis, see Fig. 3a). This orientation maximizes the electro-optic overlap, thus enhancing the modulation efficiency. To eliminate systematic errors associated with mode mismatch loss in the curved sections, the geometry of each spiral was constrained to include the same number of bends. This design ensures that the power variation between different spirals is solely a function of the propagation distance along the y-axis, providing a reliable loss measurement. Figure 3b illustrates the propagation loss as a function of wavelength, spanning from the UV to the visible spectrum. The inset displays the linear fitting used to extract the loss at 375 nm, confirming a loss of 7.2 dB/cm for a single-mode LT waveguide in this regime. This waveguide is also characterized at visible wavelengths of 488 nm and 780 nm, with propagation losses of 4.10 ± 0.3 and 2.0 ± 0.1 dB/cm, respectively. While the propagation loss increases rapidly from a wavelength of 780 nm to the UV due to enhanced scattering, the total insertion loss of the modulator remains at the same level as the associated device footprint scales down accordingly. To characterize the performance of the 1 × 2 MMI splitters, an MMI tree structure is utilized to extract the insertion loss through a linear fit of the output power versus the number of cascaded stages (Fig. 3c). The measured insertion loss of 3.25 dB per MMI, which includes the intrinsic 3 dB splitting ratio, aligns well with the simulated value of 3.11 dB. Taking into account the insertion loss of MMI and propagation loss of the waveguide, the modulator with a device length of 1.16 mm shows an insertion loss of 2.8 dB. The intrinsic optical quality of the TFLT layer was investigated via prism-coupling on a 600-nm thick TFLT wafer. By exciting the fundamental TE slab mode, a visible propagation path exceeding 7 cm can be observed in Fig. 3d. Figure 3e displays the log-scale intensity of the scattered light as a function of the propagation length. The linear fit of this experimental data reveals an attenuation of 1.32 dB/cm at 443 nm. With a measured surface roughness below 0.5 nm, the majority of the observed optical attenuation is attributed to the fundamental properties of the thin-film lithium tantalate. The propagation loss of 1.32 dB/cm at 443 nm thus represents the intrinsic absorption floor of the current TFLT wafer, providing a critical benchmark for the material performance limits as we transition into the UV. TFLT waveguide can be further improved by annealing in an oxygen atmosphere at 520 °C to repair crystal defects and reduce material absorption after processing, which is not performed in this work but will be investigated in future work[36]. In addition, scattering losses can be further mitigated by reducing the core-cladding refractive index contrast via a SiO_2 top cladding and minimizing sidewall roughness through optimized hard-mask etching.

Electro-optical performance of UV lithium tantalate modulator

The electro-optic performance of the modulator was evaluated by measuring the half-wave voltage V_π and EOE bandwidth. Figure 4a shows the measurement setup diagram used for characterizing the half-wave voltage of the modulator. A UV diode laser of 375 nm is coupled to a single mode fiber with an output power of 7 mW. A fiber polarization controller (FPC) tunes the polarization of light in the fiber to enable transverse electric (TE) mode excitation in the LT waveguide. As the phase modulator is configured to modulate TE mode only, any residual light of transverse magnetic (TM) polarization lowers the extinction ratio of the modulator. The output is collected by a single mode fiber and coupled to an avalanche photodiode (APD, APD410, Menlo Systems) for the response measurement of the modulator. Figure 4b shows the scattered light from LT photonic integrated circuits at an operating wavelength of 375 nm. The absence of visible intensity decay along the propagation indicates the low insertion loss of the modulator. Although the electrode spacing is as small as 1.5 µm, the material absorption induced by the 200 µm-long metal electrode is less than 0.01 dB in simulation, as shown in Fig. 4e. When conducting the measurement of the extinction ratio of modulators, a powermeter (S120VC, Thorlabs) is used to measure the optical power when the voltage linearly increases from 0 to 10 V. The measured extinction ratio is as high as 22.7 dB as shown in Fig. 4c. The extinction ratio is determined to be 19.4 ± 3.8 dB over six devices, suggesting a highly robust fabrication process. For scenarios requiring high extinction ratios exceeding 40 dB, modulating at longer wavelengths followed by frequency upconversion to shorter wavelengths provides an alternative route to UV optical control[37].

To investigate V_π of each modulator, a triangular signal of 400 kHz is applied on the electrodes to eliminate the impact of thermal and direct current (DC) drift. Figure 4d shows the relation among the applied signal, modulator response and time. The V_π of the modulator was determined to be 4.2 V, calculated by measuring the voltage swing required to transition the optical response between its minimum and maximum transmission points. Given an electrode length of 200 µm, this corresponds to a low $V_\pi L$ of 85 ± 2 mV · cm. Measurements of $V_\pi L$ across six modulators yielded a standard deviation of 2 mV · cm, reflecting excellent device uniformity and fabrication process

https://doi.org/10.1038/s41467-026-78862-6

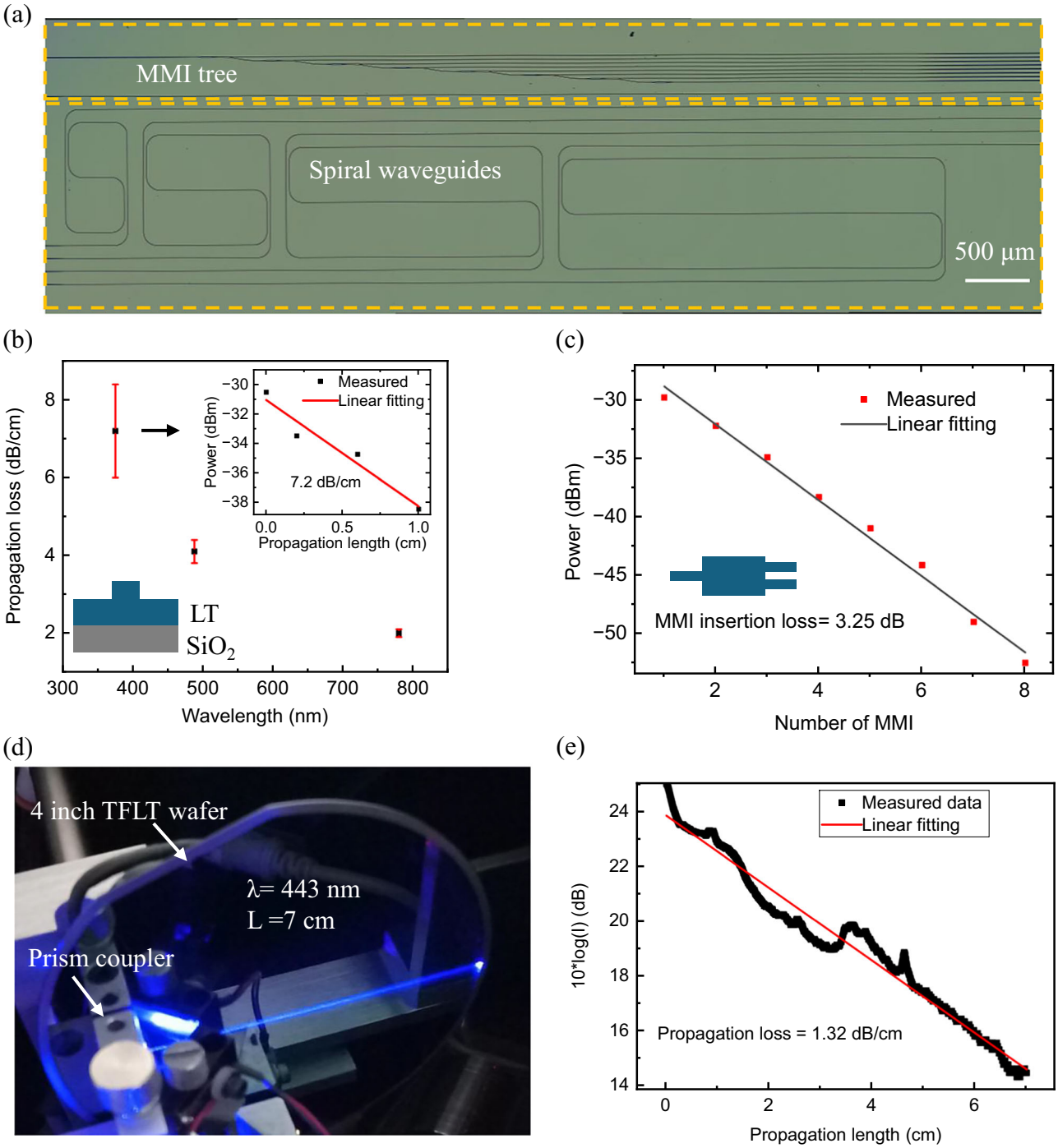


Fig. 3 | Thin-film lithium tantalate (TFLT) component characterization. **a** Optical image of the fabricated chip with multi-modal interferometer (MMI) trees and spiral waveguides for loss measurement. **b** Relationship between the propagation loss of the LT waveguides and operating wavelengths. The inset shows the linear fitting of measured intensity over propagation length at a wavelength of 375 nm. **c** The relationship between the intensity and the number of MMIs. **d** Photo of the light path in a 600 nm thick TFLT wafer at a wavelength of 443 nm. **e** Relationship between the scattered intensity (I) along the propagation length, obtained from (**d**). The loss of the thin film is estimated to be 1.32 dB/cm at 443 nm.

reproducibility. These experimental results match well with the simulation, with $V_\pi L$ directly proportional to the gap width between metal electrodes, as shown in Fig. 4e. Such a low $V_\pi L$ of 85 ± 2 mV · cm is more than one order of magnitude lower than that in telecom wavelengths(1310/1550 nm)[28,29,38]. This improvement is attributed to the shorter operating wavelength, higher material EO coefficient and stronger mode confinement in the UV. This experimental value is slightly lower than the simulated value of 96 ± 2 mV · cm. This discrepancy may result from deviations between the simulated and fabricated structures, including a larger effective Pockels coefficient than the value assumed in the simulations, a reduced electrode gap in the fabricated device, or a combination of these factors. A Pockels coefficient *r*33 of 35 pm/V is used in the simulation at the operating wavelength of 375 nm[27].

The dramatic reduction in $V_\pi L$ enables operation with an interaction length as short as 200 μm for a V_π of 4.2 V. This short interaction

https://doi.org/10.1038/s41467-026-78862-6

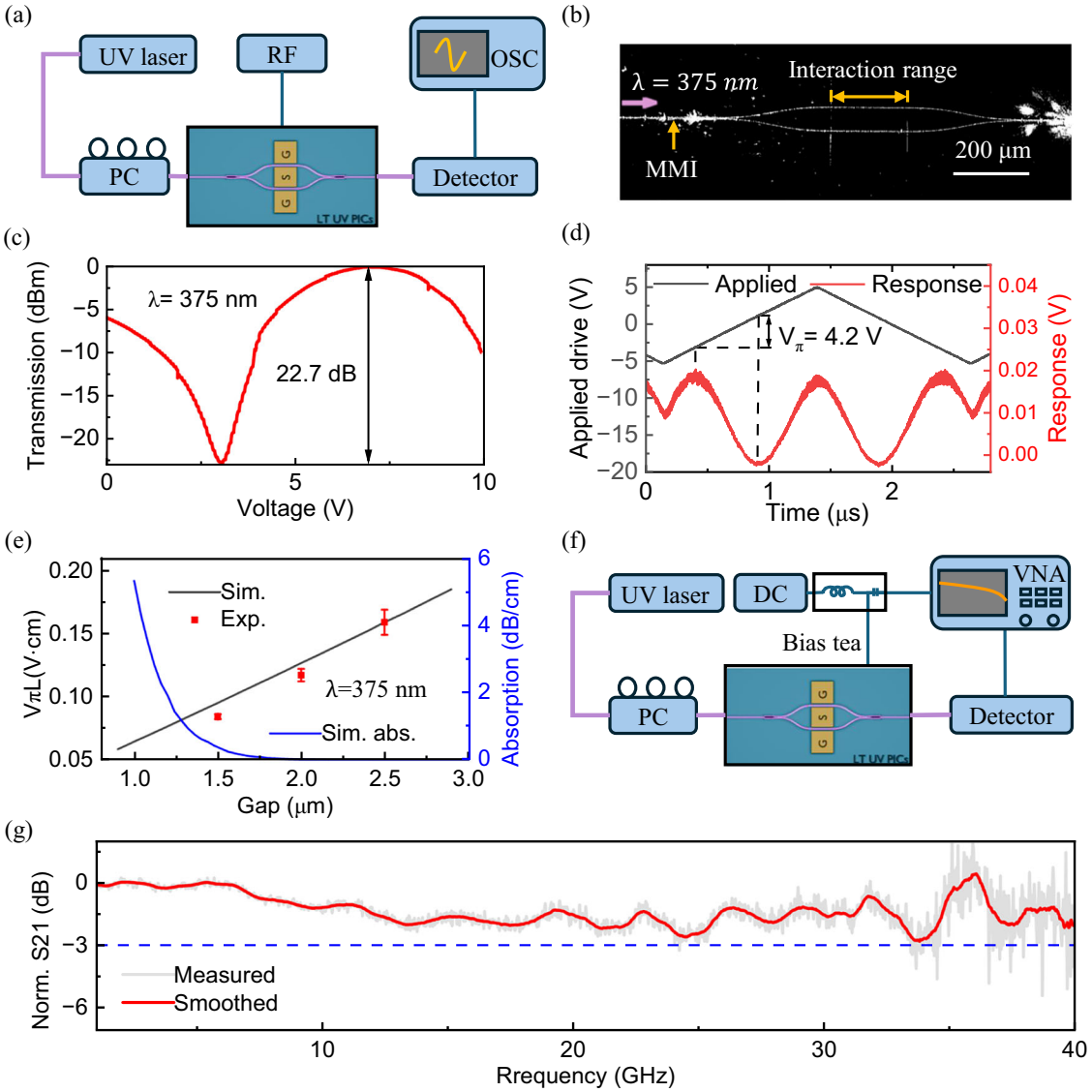


Fig. 4 | Electrical-to-optical-to-electrical (EOE) response of the thin-film lithium tantalate UV modulator. a Measurement setup used for V_π measurement. **b** Top microscope image of light at 375 nm propagating in the UV modulator. **c** Normalized transmitted power at the output port of the modulator as a function of the applied voltage. An extinction ratio of 22.7 dB is obtained. **d** The relationship between the applied triangular signal and the modulator response. The triangular wave has a frequency of 400 kHz and an amplitude of 10 V. The V_π of 4.2 V is measured in a push-and-pull configuration with a ground-signal-ground electrode. **e** Relationship between the $V_\pi L$ and electrode gap in simulation and experiments at a wavelength of 375 nm. The blue curve indicates the relationship between the simulated absorption loss and the electrode spacing. **f** Measurement setup to obtain the EOE frequency response measurement of the modulator. **g** EOE frequency response of the UV thin-film lithium tantalate modulator after de-embedding.

length, in turn, reduces on-chip insertion loss while significantly simplifying the design of high-speed electrodes because the velocity matching requirement is drastically reduced. At these ultra-short scales, the effect of velocity mismatch between the optical and the microwave mode becomes negligible, enabling efficient, high-speed modulation without the dispersion penalties typically encountered in centimeter-scale NIR devices. Due to the limited responsivity of UV-sensitive photodiodes and the moderate power levels of available laser sources, a photo-receiver module with an integrated transimpedance amplifier (TIA) was used to ensure a robust signal for the S_{21} EOE response characterization. The experimental setup for the high-speed characterization is detailed in Fig. 4f. A Vector Network Analyzer (VNA, ZNA43, Rohde & Schwarz) is used to measure the EOE frequency response of the TFLT modulator at a wavelength of 375 nm. The electrodes were terminated with a 50 Ω load using a 40 GHz RF probe (T40A GSG100, MPI) in the measurement. Figure 4g shows the EOE response of the modulator after de-embedding the photo-receiver response. A 3-dB EOE bandwidth surpassing 40 GHz is experimentally demonstrated on this modulator.

Although the EOE characterization is currently constrained by the available equipment, the electrical-to-electrical (EE) response of the electrodes was characterized using a VNA up to 67 GHz (Keysight N5247B) to evaluate the intrinsic microwave properties of the TFLT UV modulator. The measurement configuration and the corresponding simplified equivalent circuit are illustrated in Fig. 5a, b, respectively. As shown in Fig. 5c, the measured S_{21} transmission response exhibits a low microwave attenuation of only 2 dB at 67 GHz. To further explore the electrode properties, the characteristic impedance and microwave refractive index n_{RF} were extracted from the measured S-parameters to estimate EOE response(Fig. 5d–f). Because of the quasi-TEM nature of coplanar waveguide electrodes, the characteristic impedance is a stable 23 Ω across the frequency range (Fig. 5d). This indicates that the

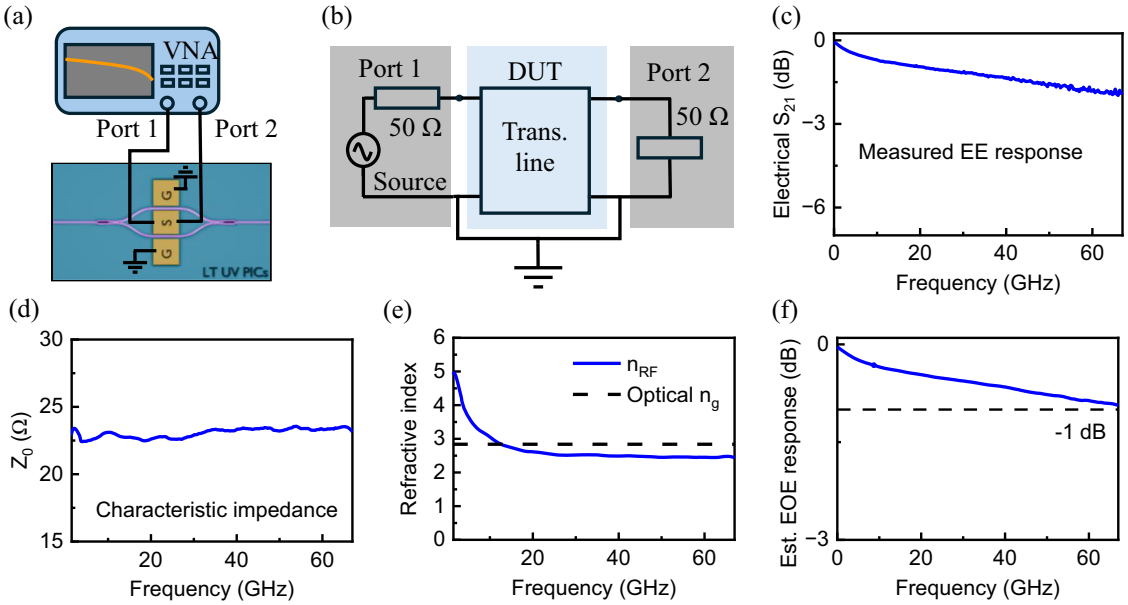


Fig. 5 | Electrical-to-electrical (EE) response of thin-film lithium tantalate UV modulator. a Measurement setup to obtain the EE response. **b** Schematic model of the measurement setup in (**a**). **c** Measured S_{21} transmission response up to 67 GHz. **d** Extracted characteristic impedance ($[Z_0]$) as a function of frequency. **e** Effective microwave refractive index n_{RF} versus frequency; the dashed line indicates the calculated optical group index n_g of the UV guided mode. **f** Estimated intrinsic EOE response. The blue and black solid curves isolate the contributions from RF loss and velocity mismatch, respectively.

modulation bandwidth could be further optimized by terminating the electrodes with a 23 Ω load to exclude any reflections at the open end of the electrodes. While high-speed modulation in traveling-wave architectures typically requires rigorous phase matching between microwave and optical fields, this device operates in a regime where the effective microwave index of 2.3 and optical group index of 2.8 are close to each other (Fig. 5e). This index control remains a critical asset for scaling to longer traveling-wave phase modulators, which are essential for applications such as UV frequency comb generation. Given the ultra-compact 200 µm interaction length of this modulator, the velocity mismatch is effectively negligible, as corroborated by the EOE response estimated from the EE electrode characterization. As shown in Fig. 5f, this EOE response is estimated by taking into account the RF loss, the velocity mismatch between the optical mode and microwave mode, and the impedance matching by terminating with 23 Ohm to minimize reflections, based on the measured EE response[39]. The estimated EOE roll-off is 1 dB at a microwave frequency of 67 GHz, far below the 3 dB threshold. The measured EOE response shown in Fig. 4g exhibits a faster roll-off than the simulated curve in Fig. 5f, which can likely be attributed to the de-embedding procedure. As the photodetector (RXM42AF, Thorlabs) is primarily calibrated for near-infrared wavelengths, its optoelectrical response may deviate in the ultraviolet regime.

Discussion

Our integrated UV EO modulator represents a significant leap over state-of-the-art platforms in terms of footprint, modulation efficiency, and high-speed potential. As illustrated in Fig. 6, we compare the $V_\pi L$ of our TFLT modulator against existing integrated modulators spanning the visible and UV regimes[40,41]. TFLN has emerged as a frontrunner for integrated EO modulators in the NIR and visible regimes, achieving a $V_\pi L$ of 0.17V · cm at 450 nm [20]. However, as the operational wavelength shifts toward the UV, TFLN faces severe limitations due to the photorefractive effect[26,42]. This effect scales aggressively at shorter wavelengths and higher optical powers, fundamentally hindering the reliability of TFLN for UV applications. TFLT has recently been shown to support watt-level high-power handling at 775 nm[38]. While TFLT electro-optic modulators have previously demonstrated high-speed performance at telecom and green (532 nm) wavelengths, our work realizes an integrated EO modulator operating in the UV at 375 nm (Fig. 6a). Besides, this modulator can also achieve high modulation efficiency at visible wavelengths. Simultaneous operation in the UV and visible range can be achieved by incorporating broadband MMIs to minimize the insertion loss across both spectral bands. We report a record-low $V_\pi L$ of 0.085 V · cm at 375 nm and 0.12 · cm at 448 nm. To the best of our knowledge, these values represent the highest modulation efficiencies achieved in the UV-visible spectrum to date. A comparative analysis of the integrated UV modulation landscape is presented in Fig. 6b. While thermo-optic (TO) modulators offer high integration density and broad spectral coverage due to their simplistic architecture, their operational speeds are fundamentally capped at the tens of kHz regime by thermal diffusion times[12]. More recently, piezoelectric-based intensity modulators on AlN-on-AlO_x platforms have demonstrated a significant leap in performance, pushing bandwidths into the tens of MHz range. While electro-optic modulation at tens of GHz is a cornerstone of modern NIR telecommunications, extending this performance to the UV has remained challenging. Traditional UV-transparent crystals such as BBO and KDP are currently restricted to bulky geometries that are incompatible with wafer-scale fabrication. Their weak light-matter interaction results in prohibitive $V_\pi L$ values in the kV · cm range and bandwidths capped at 100 MHz. In contrast, bulk lithium niobate modulators leverage a superior EO coefficient to achieve $V_\pi L$ values in the tens of V · cm. However, their intensity modulation bandwidth is frequently thermal-limited to ~ 160 MHz due to the high RF drive powers required for bulk electrodes. Furthermore, the photorefractive effect in LN constrains the input power density to below 0.5 W/mm² (AM8-UV, QuBIG Inc.), severely limiting its utility in high-brightness UV applications.

In this work, the integrated LT modulator demonstrated a low $V_\pi L$, a high bandwidth larger than 40 GHz, and a low insertion loss of 2.8 dB. Crucially, the platform exhibits optical stability. No photodarkening was observed at an on-chip optical intensity of 5 kW/mm² for 5 min, calculated from a 700 µW guide power confined within a sub-wavelength mode volume of 0.14 µm². To contextualize the

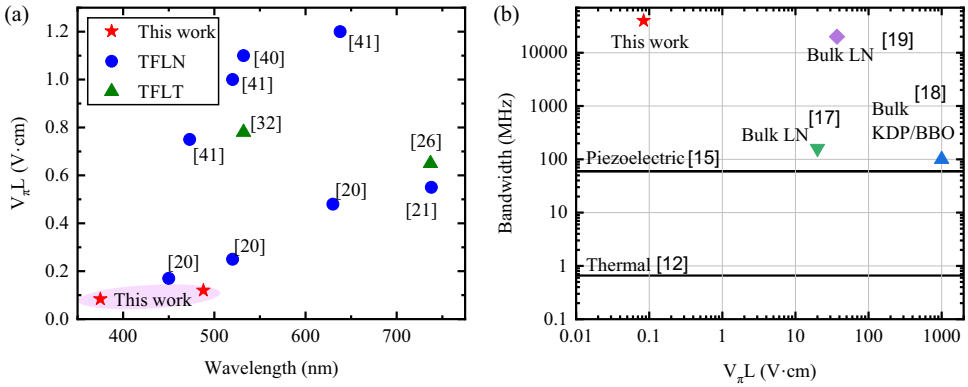


Fig. 6 | Performance benchmarks for state-of-the-art integrated electro-optic modulators in UV and visible wavelengths. a $V_\pi L$ as a function of operating wavelength across the UV and visible spectra, reported in this work and state-of-the-art integrated modulators[20,21,26,32,40,41]. **b** Comparison between this work, reported on-chip devices[12,15] and commercial bulk devices[17–19] operating at UV wavelengths, in terms of modulation bandwidth and $V_\pi L$.

performance of this device, we compare our results with other previously demonstrated on-chip and commercial bulk UV modulators in terms of bandwidth and $V_\pi L$ (bandwidth/$V_\pi L$ ratio) in Fig. 6b. By this metric, our TFLT modulator demonstrates a two-order-of-magnitude improvement over the bulk lithium niobate modulator and a five-order-of-magnitude improvement over the traditional bulk modulator made of BBO/KDP crystals.

Furthermore, this work realizes an UV photonic integrated circuit based on the thin-film lithium tantalate platform. While purely passive platforms such as AlO_x currently offer lower attenuation (<1 dB/cm) in the UV[5,10], they lack the intrinsic EO properties required for ultra-fast signal processing. By contrast, the high EO coefficient of TFLT enables a unique synergy of high-speed modulation and potential frequency conversion that is unattainable in passive thin-film oxides. Heterogeneous integration of TFLT on the passive platform via micro-transfer printing is a promising approach to combine the advances of TFLT and AlO_x platforms. This method has been demonstrated to enrich the functionality of the passive SiN platform at telecom wavelengths[31]. However, it still remains challenging to integrate LT on AlO_x because the large index contrast between TFLT and AlO_x requires a much smaller taper to ensure a low-loss transition between AlO_x and LT waveguides. In this work, by establishing a new paradigm for the integration of active UV optoelectronic devices using the TFLT platform, the challenges of device miniaturization and high-speed modulation in the UV spectrum have been addressed. The reported $V_\pi L$ of 85 mV · cm and beyond 40 GHz EOE bandwidth capability provide a scalable architecture for wafer-scale UV integrated photonics. These results enable the transition from lab-scale bulk optical setups to robust, chip-scale systems, including on-chip trapped-ion quantum computing, portable atomic clocks, UV spectroscopy, and high-bandwidth solar-blind UV communications.

Methods

Fabrication

The UV photonic integrated circuits are patterned on top of a commercial x-cut 300 nm thick thin film lithium tantalate ordered from NanoLN Inc. A 200 nm thick SiO_2 layer is deposited on top of the TFLT as a hard mask using inductively coupled plasma-enhanced chemical vapor deposition (ICP-PECVD). The photonic circuits are firstly patterned on the resist (ARP6200.13) via electron beam lithography (EBL) and then transferred to the SiO_2 layer by reactive ion etching (RIE). The etching of lithium tantalate is realized by wet chemical etching in a mixture solution of citric acid/KOH/H_2O_2 at a temperature of 85 °C. Finally, the SiO_2 hard mask is removed in buffered Hydrogen fluoride (HF) solution to complete the fabrication of LT waveguides.

The electrodes are produced by a lift-off process. The 800 nm thick resist (ARP6200.18) is patterned by EBL. After depositing a 220 nm-thick Ti/Au metal stack via electron beam physical vapor deposition (EB-PVD), the sample is immersed in ARP600-71 solution to implement the lift-off process. The sample is then diced, and the side facets are polished to maximize the coupling efficiency.

Simulation

The coupling loss between the single mode fiber and lithium tantalate waveguides is simulated with a finite difference eigenmode (FDE) solver (Lumerical, Ansys). The modal field diameter of the single mode fiber is set to 2.3 μm at the working wavelength of 375 nm. The fiber modal field diameter varies in a range of 2.0 to 2.4 μm according to the manufacturer. The waveguide width of the LT waveguide is tapered to 2.7 μm at the facet. The coupling loss is determined by the mode mismatch between the modes of the optical fiber and LT waveguides.

Measurement

The optical quality of TFLT is estimated by measuring the absorption loss of 600 nm thick four-inch TFLT wafer via the Metricon 2010/M prism coupling setup. A blue laser at an operating wavelength of 443 nm is used to investigate the material absorption of TFLT. The light is coupled to the fundamental TE mode of the slab mode in the thin film. The intensity of the scattered light is measured via a detector that scans along the propagation path and records the intensity of scattered light. As the top surface of the thin film has a negligible surface roughness of 0.2 nm, the measured loss is mainly attributed to the absorption of the layer. The loss is obtained by implementing linear fitting of the log-scale intensity over the propagation length, as shown in Fig. 3e.

To characterize propagation loss at visible wavelengths, 488 nm (OBIS 488LX, Coherent) and 780 nm (DL Pro 780, Toptica) single-mode fiber-coupled lasers were used. Light was coupled into the integrated LT waveguides using lensed fibers (OZ Optics), and the output power was recorded with a power meter (S120VC, Thorlabs). The on-chip insertion loss at 375 nm was determined to be 2.8 ± 0.6 dB by subtracting the total fiber-to-chip coupling loss from the measured fiber-to-fiber insertion loss. This value exceeds the theoretical prediction of 1.3 dB, which is calculated from the measured waveguide propagation loss and MMI insertion losses, potentially due to the combined effect of the electrode misalignment and the deviation of fiber-to-chip coupling efficiency in measurement.

Data availability

Relevant data supporting the key findings of this study are available within the article.

References

1. Corsetti, S. M. et al. Integrated-photonics-based systems for polarization-gradient cooling of trapped ions. *Light Sci. Appl.* **15**, 57 https://doi.org/10.1038/s41377-025-02094-4 (2026).
2. Mehta, K. K. et al. Integrated optical multi-ion quantum logic. *Nature* **586**, 533–537 https://doi.org/10.1038/s41586-020-2823-6 (2020).
3. Kwon, J. et al. Multi-site integrated optical addressing of trapped ions. *Nat. Commun.* **15**, 3709 https://doi.org/10.1038/s41467-024-47882-5 (2024).
4. Xu, B., Chen, Z., Hänsch, T. W. & Picqué, N. Near-ultraviolet photon-counting dual-comb spectroscopy. *Nature* **627**, 289–294 https://doi.org/10.1038/s41586-024-07094-9 (2024).
5. Lin, C. et al. UV photonic integrated circuits for far-field structured illumination autofluorescence microscopy. *Nat. Commun.* **13**, 4360. https://doi.org/10.1038/s41467-022-31989-8 (2022).
6. Lin, C., Schaubroeck, D., Baets, R., Boon, N. & Thomas, N. L. UV photonic-integrated-circuits-based structured illumination microscopy with a field of view larger than 100 μm^2. In *IEEE Journal of Selected Topics in Quantum Electronics* **29** https://doi.org/10.1109/JSTQE.2023.3243776 (IEEE, 2023)
7. Mo, X. et al. Solar-blind deep ultraviolet light communication network. *Opt. Express* **33**, 36280–36292 https://doi.org/10.1364/oe.570896 (2025).
8. Sun, X. et al. 375-nm ultraviolet-laser based non-line-of-sight underwater optical communication. *Opt. Express* **26**, 12870—12877 https://doi.org/10.1364/oe.26.012870 (2018).
9. Brown, K. R., Chiaverini, J., Sage, J. M. & Häffner, H. Materials challenges for trapped-ion quantum computers. *Nat. Rev. Mater.* **6**, 892—905 https://doi.org/10.1038/s41578-021-00292-1 (2021).
10. Neutens, P. et al. A 200 mm wafer-scale al2o3 photonics waveguide technology for UV and visible applications. *IEEE Photonics J.* **17** https://doi.org/10.1109/JPHOT.2025.3568162 (2025).
11. Hendriks, W. A. P. M., Bonneville, D. B., Mardani, S., Dijkstra, M. & Garcia-Blanco, S. M. UV integrated photonics in sputter deposited aluminum oxide https://doi.org/10.1364/opticaopen.25663656.v1 (2024).
12. Wang, H. et al. Highly efficient thermo-optic phase shifters for UV photonic applications. *Opt. Express* **34**, 7758–7769 https://doi.org/10.1364/oe.582592 (2026).
13. Li, K. et al. An integrated cmos-silicon photonics transmitter with a 112 gigabaud transmission and picojoule per bit energy efficiency. *Nat. Electron.* **6**, 910–921 https://doi.org/10.1038/s41928-023-01048-1 (2023).
14. Liu, X. et al. Ultra-high-Q UV microring resonators based on a single-crystalline aln platform. *Optica* **5**, 1279–1282 https://doi.org/10.1364/optica.5.001279 (2018).
15. Castillo, Z. A. et al. Cmos-fabricated ultraviolet light modulator using low-loss alumina piezo-optomechanical photonics. *Opt. Quantum* **4**, 114–120 https://doi.org/10.1364/OPTICAQ.582412 (2026).
16. Picqué, N. & Hänsch, T. W. Frequency comb spectroscopy. *Nat. Photonics* **13**, 146–157 https://doi.org/10.1038/s41566-018-0347-5 (2019).
17. QUBIG GmbH: AM8-UV amplitude modulator. https://www.qubig.com/products/electro-optic-modulators_eom/amplitude-modulators_am/am8-uv. Accessed: 2026-04-14 (2026).
18. QUBIG GmbH: PC-UV Pockels cell. https://www.qubig.com/products/electro-optic-modulators_eom/pockels-cells_pc/pc-uv. Accessed: 2026-04-14 (2026).
19. QUBIG GmbH: PM11-UV phase modulator. https://www.qubig.com/products/electro-optic-modulators_eom/phase-modulators_pm/pm-free-space_pm-bulk/pm11-uv. Accessed: 14 April 2026.
20. Xue, S. et al. Full-spectrum visible electro-optic modulator. *Optica* **10**, 125–126 https://doi.org/10.1364/optica.482667 (2023).
21. Renaud, D. et al. Sub-1 volt and high-bandwidth visible to near-infrared electro-optic modulators. *Nat. Commun.* **14**, 1496. https://doi.org/10.1038/s41467-023-36870-w (2023).
22. Achuthan, N. et al. Broadband electro-optic modulation at blue wavelengths in thin-film lithium niobate. in *Photonics for Quantum 2025* (eds Reimer, M. & Rotenberg, N) vol. 13563, Bellingham https://doi.org/10.1117/12.3062752 (SPIE, 2025).
23. Franken, C. A. A. et al. Millawatt-level UV generation using sidewall poled lithium niobate. *Nat. Commun.* **17**, 3651 https://doi.org/10.1038/s41467-026-68524-y (2026).
24. Alexandrovski, A. L., Foulon, G., Myers, L. E., Route, R. K. & Fejer, M. M. UV and visible absorption in litao 3. in *Laser Material Crystal Growth and Nonlinear Materials and Devices*, vol. 3610 https://doi.org/10.1117/12.349242 (SPIE, 1999).
25. Zverev, G. M., Levchuk, E. A., Pashkov, V. A. & Poryadin, Y. D. Laser-radiation-induced damage to the surface of lithium niobate and tantalate single crystals. *Sov. J. Quantum Electron.* **2**, 167 https://doi.org/10.1070/QE1972V002N02ABEH004409 (1972).
26. Guo, C. et al. Robust and active visible-light integrated photonics on thin-film lithium tantalate for underwater optical wireless communications. Preprint at https://doi.org/10.48550/arXiv.2603.14346 (2026).
27. Juvalta, F., Jazbinsek, M., Günter, P. & Kitamura, K. Electro-optical properties of near-stoichiometric and congruent lithium tantalate at ultraviolet wavelengths. *JOSA B* **23**, 276–281 https://doi.org/10.1364/josab.23.000276 (2006).
28. Wang, C. et al. Lithium tantalate photonic integrated circuits for volume manufacturing. *Nature* **629**, 784–790 https://doi.org/10.1038/s41586-024-07369-1 (2024).
29. Powell, K. et al. Dc-stable electro-optic modulators using thin-film lithium tantalate. *Opt. Express* **32**, 44115–44122 https://doi.org/10.1364/OE.538870 (2024).
30. Han, H. et al. Thermo-optic characterization of thin-film lithium niobate asymmetric mach-zehnder interferometer from 290 to 10 k. *Chin. Opt. Lett.* **23**, 051302 https://doi.org/10.3788/COL202523.051302 (2025).
31. Niels, M. et al. A high-speed heterogeneous lithium tantalate silicon photonics platform. *Nat. Photonics* **20**, 225–231 https://doi.org/10.1038/s41566-025-01832-9 (2026).
32. Powell, K. et al. A sub-volt near-ir lithium tantalate electro-optic modulator. APL Photonics **10** https://doi.org/10.1063/5.0278724 (2025)
33. Ying, P. et al. Low-loss edge-coupling thin-film lithium niobate modulator with an efficient phase shifter. *Opt. Lett.* **46**, 1478, https://doi.org/10.1364/ol.418996 (2021).
34. Lin, C. et al. Ultra-low loss and large bandwidth fiber-to-chip edge coupler for aluminum oxide photonic platform at UV-visible wavelengths. *J. Lightwave Technol.* **43**, 7265—7269 https://doi.org/10.1109/JLT.2025.3567712 (2025).
35. Nenezic, P. et al. Wet etching of low loss lithium tantalate waveguides and heterogeneous lithium tantalate integration, 1–2 https://doi.org/10.1109/IPC65510.2025.11282158 (2025)
36. Shams-Ansari, A. et al. Reduced material loss in thin-film lithium niobate waveguides. *APL Photonics* **7**, 81301 https://doi.org/10.1063/5.0095146 (2022).
37. Sabatti, A. et al. Extremely high extinction ratio electro-optic modulator via frequency upconversion to visible wavelengths. *Opt. Lett.* **49**, 3870—3873 https://doi.org/10.1364/OL.525733 (2024).
38. Kuznetsov, N., Li, Z., Kippenberg, T. J.: Watt-level second harmonic generation in periodically poled thin-film lithium tantalate. Preprint at https://doi.org/10.48550/arXiv.2512.07968 (2025).
39. Witzens, J., IEEE, S. M.: High-speed silicon photonics modulators https://doi.org/10.1109/JPROC.2018.2877636 (2018).

40. Li, C. et al. High modulation efficiency and large bandwidth thin-film lithium niobate modulator for visible light. *Opt. Express* **30**, 36394–36402 https://doi.org/10.1364/OE.469065 (2022).
41. Hara, H. et al. Low voltage visible light modulation for three colors (red, green, blue) by sputtered lithium niobate thin film. *AIP Adv.* **14** https://doi.org/10.1063/5.0171734/3061495 (2024).
42. Xu, Y. et al. Mitigating photorefractive effect in thin-film lithium niobate microring resonators. *Opt. Express* **29**, 5497–5504 https://doi.org/10.1364/oe.418877 (2021).

Acknowledgements
We would like to acknowledge C. Krückel for measurement support.

Author contributions
C.L. conceived, performed, and analyzed the experiments. C.L. designed and fabricated the device. C.L. and T. V. simulated the V_π of the device. C.L., P.N., M.N., V.B.O., and M.B. developed the waveguide process flow, K. A. measured the TFLT absorption loss, C.L., S.C., S.A., H.L., and A.M. measured the high-speed response of the device. X.Y. supported the EOE measurement. The project was supervised by B.K. All authors reviewed and approved the manuscript.

Funding
This work is supported by Horizon Europe Project Qu-PIC (101135845).

Competing interests
The authors declare no competing interests.

Additional information
Supplementary information The online version contains supplementary material available at https://doi.org/10.1038/s41467-026-78862-6.

Correspondence and requests for materials should be addressed to Chupao Lin.

Peer review information *Nature Communications* thanks the anonymous reviewer(s) for their contribution to the peer review of this work. A peer review file is available.

Reprints and permissions information is available at http://www.nature.com/reprints

Publisher's note Springer Nature remains neutral with regard to jurisdictional claims in published maps and institutional affiliations.

Open Access This article is licensed under a Creative Commons Attribution 4.0 International License, which permits use, sharing, adaptation, distribution and reproduction in any medium or format, as long as you give appropriate credit to the original author(s) and the source, provide a link to the Creative Commons licence, and indicate if changes were made. The images or other third party material in this article are included in the article's Creative Commons licence, unless indicated otherwise in a credit line to the material. If material is not included in the article's Creative Commons licence and your intended use is not permitted by statutory regulation or exceeds the permitted use, you will need to obtain permission directly from the copyright holder. To view a copy of this licence, visit http://creativecommons.org/licenses/by/4.0/.

© The Author(s) 2026

This Article in Press is shared early to give you faster access to new research. It is citable and carries a permanent DOI. The final edited version will replace it automatically.